doi:10.26443/seismica.v2i2.247

Spatiotemporal evaluation of Rayleigh surface waves estimated from roadside dark fiber DAS array and traffic noise

Rafał Czarny * [1], **Tieyuan Zhu** [1], **Junzhu Shen** [1]

[1]Department of Geosciences, The Pennsylvania State University, University Park, United States

Author contributions: *Conceptualization*: R. Czarny. *Data Curation*: R. Czarny, T. Zhu. *Formal Analysis*: R. Czarny. *Funding Acquisition*: T. Zhu. *Investigation*: R. Czarny, T. Zhu. *Methodology*: R. Czarny. *Project Administration*: R. Czarny, T. Zhu. *Resources*: T. Zhu. *Software*: R. Czarny, J. Shen. *Supervision*: T. Zhu. *Validation*: R. Czarny. *Visualization*: R. Czarny. *Writing – original draft*: R. Czarny, T. Zhu. *Writing – review & editing*: R. Czarny, T. Zhu, J. Shen.

Abstract Seismic imaging and monitoring of the near-surface structure are crucial for the sustainable development of urban areas. However, standard seismic surveys based on cabled or autonomous geophone arrays are expensive and hard to adapt to noisy metropolitan environments. Distributed acoustic sensing (DAS) with pre-existing telecom fiber optic cables, together with seismic ambient noise interferometry, have the potential to fulfill this gap. However, a detailed noise wavefield characterization is needed before retrieving coherent waves from chaotic noise sources. We analyze local seismic ambient noise by tracking five-month changes in signal-to-noise ratio (SNR) of Rayleigh surface wave estimated from traffic noise recorded by DAS along the straight university campus busy road. We apply the seismic interferometry method to the 800 m long part of the Penn State Fiber-Optic For Environment Sensing (FORESEE) array. We evaluate the 160 virtual shot gathers (VSGs) by determining the SNR using the slant-stack technique. We observe strong SNR variations in time and space. We notice higher SNR for virtual source points close to road obstacles. The spatial noise distribution confirms that noise energy focuses mainly on bumps and utility holes. We also see the destructive impact of precipitation, pedestrian traffic, and traffic along main intersections on VSGs. A similar processing workflow can be applied to various straight roadside fiber optic arrays in metropolitan areas.

Production Editor: Gareth Funning
Handling Editor: Nicola P. Agostinetti
Copy & Layout Editor: Jack B. Muir

Received: May 15th, 2023
Accepted: July 6th, 2023
Published: August 14th, 2023

1 Introduction

To develop and reinforce urban infrastructure for smart cities, the number of fiber optic cable installations rapidly increases. Recent studies show that these networks can be used not only for communication and transferring data but also for monitoring and imaging the near-surface structure using DAS (Li et al., 2022). For rapidly growing urban population densities, shallow subsurface characterization of physical and mechanical properties regarding groundwater resources management, infrastructure safety, road inspection, or geohazards monitoring is crucial for sustainable development. DAS can turn the fiber optic cable into a sensor array sensitive to ground vibrations (Lindsey and Martin, 2021). Consequently, the fiber optic line can work like a geophone spread in seismic methods. This technology can operate in tough conditions like extreme temperature or power supply limitations and record vibrations within 17 octaves (Paitz et al., 2021). Therefore, it has been used simultaneously in global seismology (Nayak and Ajo-Franklin, 2021) and at a laboratory scale (Titov et al., 2022). Furthermore, it requires only a single power point source to record vibration from tens of km of fiber lines with meter-scale sampling resolution. Hence, it is less expensive and easier to maintain than a standalone geophone array, especially with the city's pre-existing dark fiber optic cables.

Ambient seismic noise, which is dominated by surface waves (Nakata et al., 2019), gives the ability to analyze elastic properties of the subsurface cost-effectively. Seismic interferometry is one of those methods which allows extracting useful information from randomly distributed sources (Wapenaar et al., 2010). This method mimics a standard seismic survey by focusing the chaotic seismic wavefield into the virtual source (VS) and then exciting it toward receivers. The main drawback of seismic interferometry application in a metropolitan area is the complex nature of the noise therein. In such conditions, the dominant noise source can be localized out of the stationary-phase region (out of line crossing virtual source-receiver pair) and produce apparent surface wave velocity. This azimuthal-dependent source distribution can be analyzed using a large-N geophone array (Nakata et al., 2015), or dense DAS array (Zeng et al., 2017; van den Ende and Ampuero, 2021). Unfortunately, many dark fibers are limited to straight-line profiles deployed close to the main roads in the city and sense only the vibrations in the direction of fiber optic cable. For such limitations, spatial noise distribution analysis of the high-frequency range noise, which can change the behavior every couple of meters, is complicated. The most common practice for such an environment is to increase the illumination time to retrieve reliable surface waves (Spica et al., 2020;

*Corresponding author: rkc5556@psu.edu

Yang et al., 2022), or use well-recognized strong local seismic sources, e.g., trains (**?**), cars (Dou et al., 2017; Song et al., 2021) or quarry blasts (Fang et al., 2020). When the noise source is more complex, one can use coda wave interferometry and scattering waves which are less sensitive to noise inhomogeneity (**?**). In a recent paper, Song et al. (2022) present the promising three-station interferometry technique, which can increase the coherence of noise correlation functions. However, estimating a stable high-frequency surface wave from ambient noise in the city remains challenging, and understanding what influences local Green's function is mandatory.

In this paper, we investigate high-frequency ambient noise behavior in time and space by analyzing the signal-to-noise ratio (SNR) of Rayleigh surface waves estimated from traffic noise recorded by the Penn State Fiber-Optic For Environment Sensing (FORESEE) array in State College, Pennsylvania. We utilize an 800 m straight profile of telecom fiber along Pollock Rd, one of the busiest university campus roads where thousands of students pass by every day during the semester. First, we characterize the ambient seismic noise through the city. Then we analyze 160 virtual shots gathers (VSGs) from the beginning of May to the end of September 2019. We recognize the main factors determining the SNR of Rayleigh surface waves along the road. We also characterize noise source distribution in space using back projection technique. Our method can be used for other sites with straight-line geometry.

2 Data characterization

2.1 The DAS Array

The Penn State FORESEE DAS array consists of 4.2 km of dark fiber that crosses the Pennsylvania State University campus (Fig. 1a). The recording started in April 2019 and finished in October 2021 with three different frequency samplings: 250 Hz, 500 Hz, and 1000 Hz (Fig. 1b). The depth of the telecom fiber optic cable varies with an average of 1 m (personal communication). The interrogator Silixa iDAS2 as sensing the 2137 channels every 2 m with a 10 m gauge length. More details about the array and observations can be found in Zhu et al. (2021). We analyze the 800 m straight segment along Pollock Rd (Fig. 1c).

2.2 Seismic ambient noise

Figure 2 presents the power spectrum density (PSD) changes over two weeks of May 2019 for 2137 channels. The PSD is averaged within four different frequency ranges: 0.5–4 Hz, 4–10 Hz, 10–20 Hz, and 20–50 Hz. For each range, the higher amplitudes start around 8 AM and end around 8 PM. The strongest noise comes from the main streets of University Dr, Curtin Rd, and Pollock Rd (Fig. 1a). However, Curtin Rd shows the highest values, especially between channels 808 and 1120, where the cable is set up close to the road shoulder. The higher PSD values in all frequency ranges for channels near the road suggest that the anthropogenic noise sources originate in traffic. During the weekends, we observe a slight PSD decrease, mainly in the lower frequency range (0.5–4 Hz), probably due to reduced heavy vehicle traffic these days. A similar pattern of anthropogenic noise emerging during the day and decaying at night (Shen and Zhu, 2021) was observed in other cities (e.g., Díaz et al., 2017).

We also observe the weather condition imprint on PSD. The wind and rain during the storm on May 4 changed the PSD in all frequency ranges. The wind amplifies PSD but only for the first 500 channels and when the wind gusts exceed 15 m/s (Fig. 2b). The first 500 channels are in the open space area near campus football pitches, where the wind can much more easily induce ground vibration than in built-up areas. During heavy rain, the PSD values increase for a few channels close to the storm sewers (Fig. 2c). The increase starts a few minutes after the beginning of the rain and vanishes a couple of minutes after the rain. It is likely the acoustic effect of fluid flowing through the drainage system (Shen and Zhu, 2023, submitted).

3 Rayleigh surface wave evaluation

3.1 Rayleigh surface wave estimation

Figure 2 shows that most of the seismic noise concentrates along the roads and is caused by traffic. Around 75 % of FORESEE DAS channels are installed beneath the sidewalks and near the road shoulders (Fig. 1). For such geometry, where the noise source propagates inline, the Rayleigh surface wave is amplified (e.g., Spica et al., 2020). However, in some heavy traffic intersections, Love surface waves can also be sensed by the DAS fiber array (Martin et al., 2018). To monitor and image the first few meters of the subsurface with the ambient noise interferometry along the straight road, we need to understand better what influences the SNR of the estimated Rayleigh surface wave in time and space. To do so, we focus on the 400 channels along Pollock Rd (from channel 1460 to 1860) (Fig. 1c). It is the longest straight part of the array within the built-up campus area. Our processing workflow is similar to what was introduced in seismology (Bensen et al., 2007) (Fig. 3).

We only modify the preprocessing step by running the same workflow for each 1-minute continuous recording input file twice for negative and positive wavenumbers. Czarny and Zhu (2022) used a similar approach for 1D S-wave velocity model estimation along Pollock Rd. This procedure gives us more information about the spatial distribution of the noise source described later. We also constrain the wavefield between phase velocity 100 m/s and 5500 m/s in the f-k domain to reduce the influence of the noise sources out of the stationary-phase region. Then, we process both wavefields separately. We detrend the data, decimate to 100 Hz sampling frequency, band-pass between 1 and 45 Hz, and flatten the spectrum using spectral whitening. Eventually, we generate VSGs with a step of 5 channels for a new VS point. It gives us 160 virtual source points (80 for each wavenumber). Following these steps, we process data from May to September 2019. To reduce

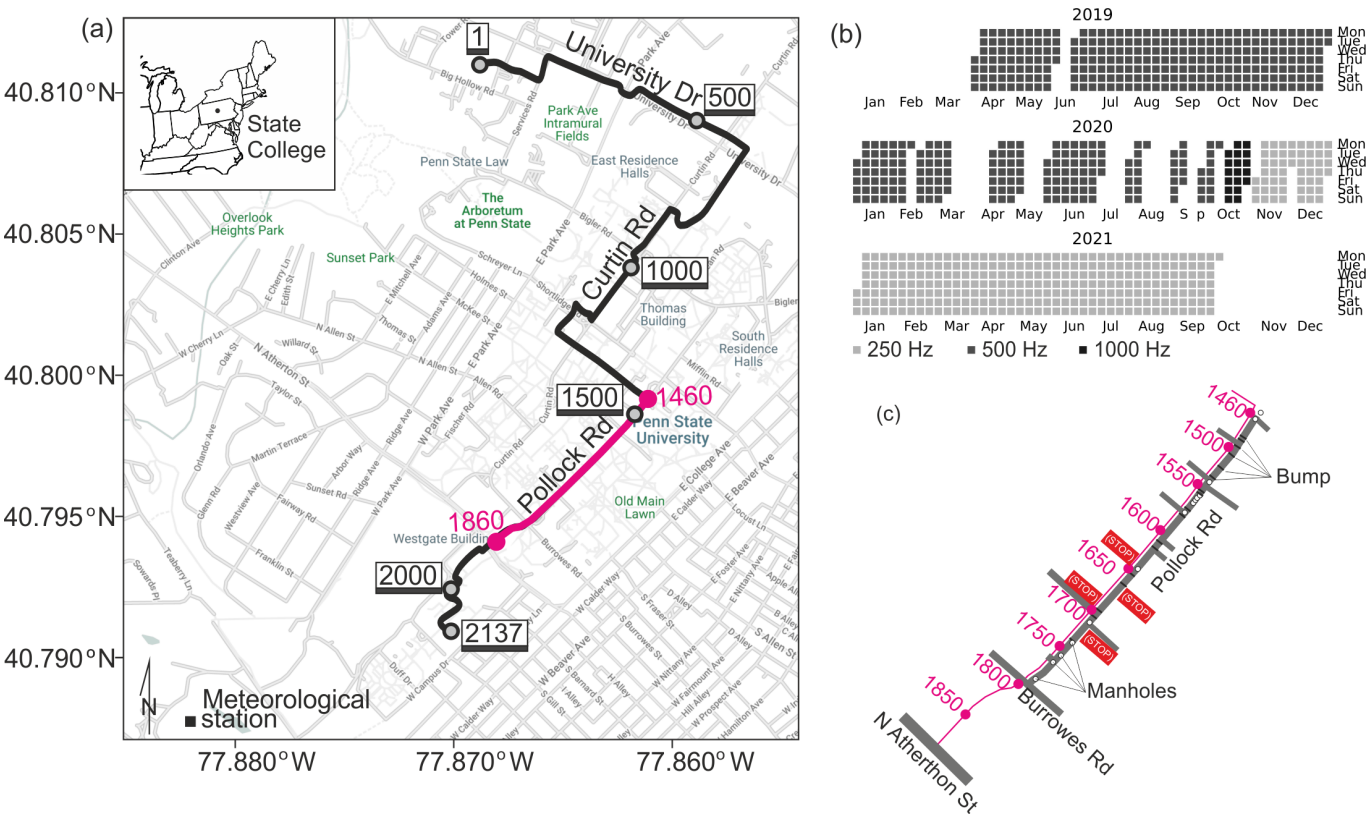

Figure 1 (a) Dark fiber DAS array layout. (b) The scope of FORESEE project recordings. (c) A part of the array (from channel 1460 to channel 1860) and the main road infrastructure we use in the study.

computation time, we take only daytime (from 8 AM to 8 PM) when the heaviest traffic occurs.

3.2 Signal-to-noise ratio

VSGs stacked over one month (Fig. 3) show that the main energy of the Rayleigh surface wave travels as a fundamental mode with an average velocity for higher frequencies (10-35 Hz) around 1120 m/s. To evaluate the SNR of the estimated Rayleigh surface wave in time and space, we use the slant-stack method (Vidal et al., 2014) and transform VSGs obtained for every 1-minute data to the slowness representation using the formula:

$$C(f,p) = \left\| \sum_{j=1}^{N} e^{i2\pi f x_j p} A\left(f, x_j\right) \right\|_{\max} \quad (1)$$

where $C(f,p)$ is the maximum value searching from the summation over different phase shifts in the frequency domain; $A\left(f, x_j\right)$ is a Fourier transform of the VSG where each j receiver has x_j offset from the VS point; p and f denote slowness and frequency, respectively. We use 100 channels around each VS. In figure 4, we present the slant-stacking summation for 3 different VSGs for the same VS point with different SNR of the estimated Rayleigh surface wave. To make analysis easier, we change slowness to phase velocity. We use the wave between 1 and 45 Hz. To assess SNR, we determine the ratio between maximum energy focused on the fundamental mode (900–1500 m/s) and the other velocities. We similarly process all VS points for positive and negative wavenumbers.

4 Results and Discussion

4.1 Temporal SNR changes

Figure 5 presents the distribution of SNRs along Pollock Rd in a daily time frame from the beginning of May to the end of September 2019, except June. Figures 5d and 5e represent VSGs for negative wavenumber (we call it negative wavefield - propagates from higher to lower channels) and VSGs for positive wavenumber (we call it positive wavefield - propagates from lower to higher channels), respectively. To better understand temporal SNR variations, we add temperature (Fig. 5b) and the precipitation (Fig. 5c) from the local meteorological station (Fig. 1a) and depth to water level (Fig. 5c) from the USGS observatory well located 4 km from our array.

Both wavefields generally show a similar pattern, but the negative one reveals higher SNR values overall. This difference is visible in Figure 5f, which represents the SNR averaged for all VS points. For all days except May 12 and 13, we notice intense illumination by the ambient noise coming from the west. It is probably seismic noise due to heavy car traffic along the 4-lane N Atherton St. that crosses the FORESEE array around channel 1880 (Fig. 1c). In Figure 5g, as a result of subtracting the SNR for negative from the SNR for positive wavefields, we can also observe how this western noise source amplifies the wavefield in almost all VS points.

SNR distribution over five months shows some long- and short-term changes. For long-term changes, we can distinguish three periods: from May 1 to May 16, May 16 to August 23, and August 23 to the end of September. During the first and last periods, the SNR decreases.

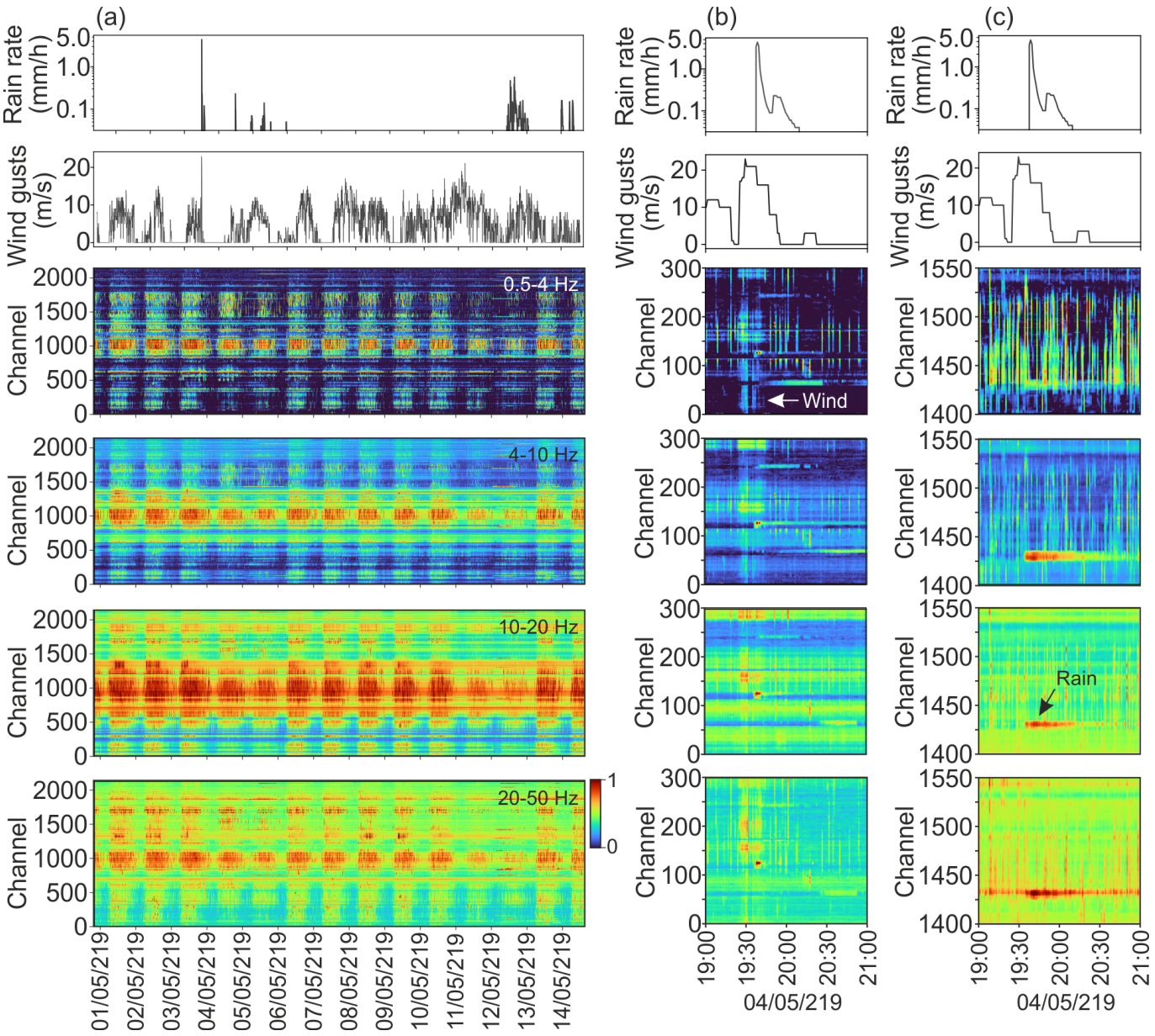

Figure 2 (a) PSD averaged in 4 frequency ranges: 0.5-4 Hz, 4-10 Hz, 10-20 Hz, and 20-50 Hz. Higher PSD values are noticed for fiber optic cable installed near the main campus roads. (b) Amplitude increase due to wind gusts for the first 500 channels located in an open-space area. (c) Amplitude increase due to water flowing through the drainage system close to the fiber optic cable conduit.

We link this drop with students' activity on the University campus during the spring and fall semesters. Pollock Rd is the main campus path for walking and riding bikes. The local high-frequency noise from pedestrians and cyclists can contaminate coherent surface wave phases from distant sources. Moreover, telecom fiber in many places is installed directly below the pavement and close to the surface, which amplifies this effect.

Short-term SNR changes are connected with weather conditions and urban activity. The SNR increases on almost all weekends, particularly during the summer break. Generally, at the weekend, the university is visited by fewer people. This pattern disturbs May 5 (Fig 5f, labeled as A), when the commencement ceremonies occurred. The beginning of the fall semester is also a time with more pedestrians at the university, even during the weekends. That is why we do not see an increase in SNR at weekends from August 23 to the mid of September.

The PSD shows that wind does not generate strong ground vibration in the build-up area (Fig. 2). However, precipitation and temperature impact the SNR. For example, between May 12 and 14, a long-hour lasting moderate precipitation occurred and changed the depth to the water level of about 50 cm in next following days (Fig. 5a). It was the highest precipitation during all five months of our analysis. As a result, the SNR significantly decreases. Interestingly, in next following two days, we observe higher average SNR for the positive wavefield (Fig. 5e, labeled as B) than the negative one. We posit that the ambient noise from N Atherton St. is attenuated more due to higher water content in the shallow surface.

In addition, in Figure 6, we present the maximum amplitudes of the Rayleigh surface wave in the range of 1-

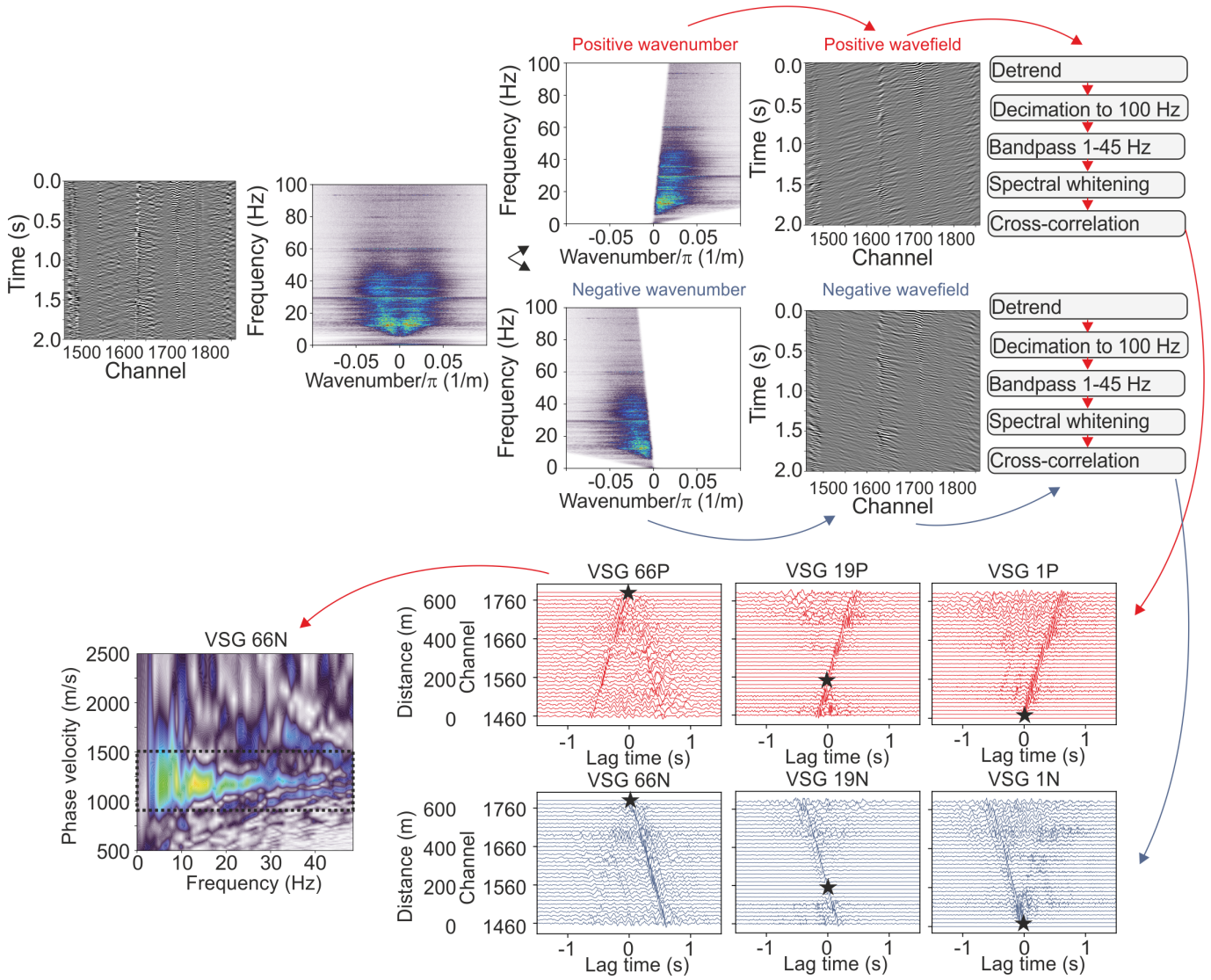

Figure 3 The processing flowchart of Rayleigh surface wave estimation from seismic ambient noise regarding the wavefield direction. The examples of VSGs obtained by linear stacking of the one-month data show consistency in Rayleigh surface wave velocity of the main energy. The fundamental model propagates between 1000-1500 m/s in the higher frequency range.

45 Hz between May 12 and May 16. These surface waves are generated by cars passing through the same bump around channel 1540. For each day, we select 8 waveforms (from 8 cars) with similar strain rate values in a source (channel below the bump). Due to the high contamination of other seismic noise to the selected wavefield, we examine only the near field around the bump. Indeed, the surface wave attenuates the most on May 12 (Fig. 6f). The attenuation can be visible on pure waveforms in Figures 6g and 6h. The amplitudes decay much faster on May 12 (wet day) than on May 16 (dry day) for comparable source energy.

We do not see such strong attenuation on May 13 and May 14 for nearfield, but only SNR drop from farfield (west noise from N Atherton St.). We hypothesize that the water did not evaporate but slowly percolated to the topsoil layer and then infiltrated into the deeper layers. It happened because of the lower temperature those days. The shallow subsurface, up to tens of meters around the campus, contains fractured dolomite above the limestone layer with karst features in this region (Drake and Harmon, 1973). The top 2 to 4 m is built with clay. Water can easily migrate through the well-developed subsurface drainage within such prone sinkhole hazards carbonate strata. However, testing this hypothesis is beyond this study's scope. It is worth noting that when a few short storms occurred at the end of May, rapidly changing the water table, the SNR (Fig. 5e, labeled as (C)) remained high when the temperature is around 20 °C in this period.

4.2 Spatial SNR changes

One-component data recorded along the straight dark fiber DAS array is challenging to characterize the noise origin in space. However, we identify the primary seismic noise sources in the investigation area using the back projection technique (e.g., Li et al., 2020; Rabade et al., 2022; Song et al., 2022). This method illuminates the most likely distribution of noise source energy in space by migrating the amplitude from the time domain VSG to the grid in space using the averaged velocity of the investigated seismic wave. First, the difference between the distance of the VS point to the grid point and

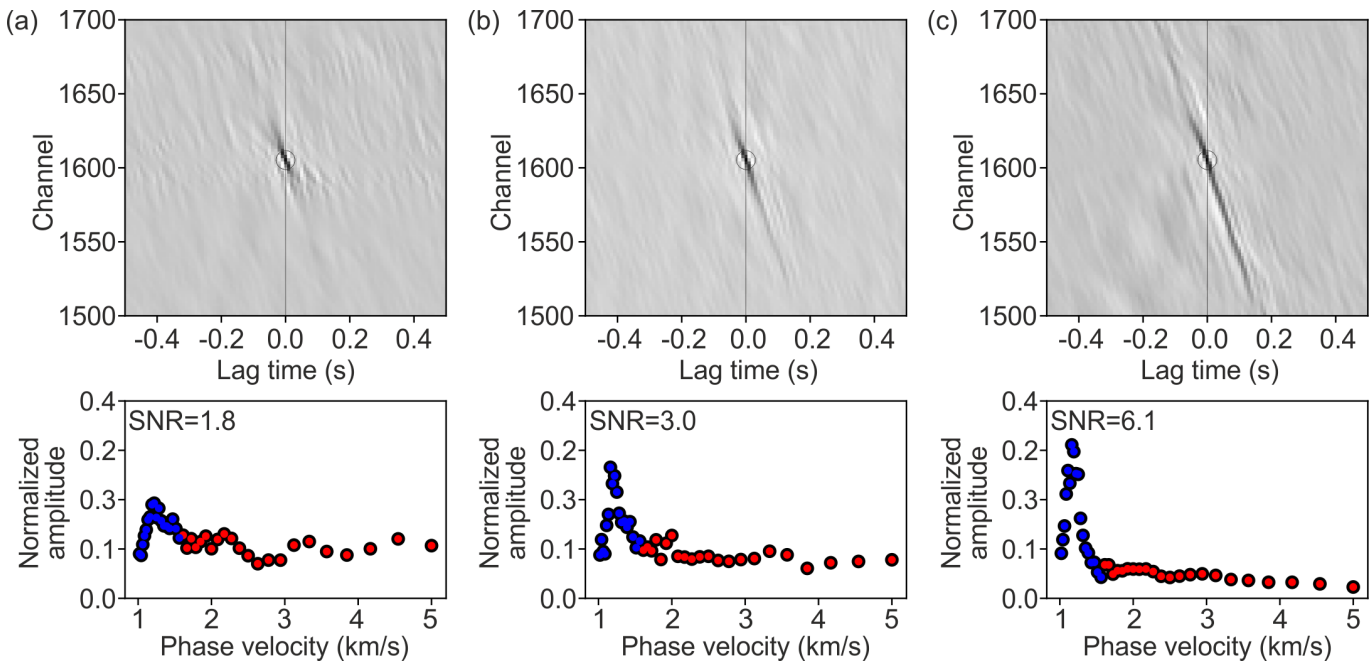

Figure 4 The slant-stack analysis examples for the same VS point but three different minutes with three different SNR of Rayleigh surface wave: 1.8, 3.0, and 6.1.

the distance of VS point to the receiver is computed. Then, for this difference, the wave is focused on the grid point using the averaged velocity. The wave energy is the root-mean-square of amplitudes in the time window with the length of the wave duration. We use the 40 ms window as an optimum parameter for our array. This window corresponds to the duration of the fundamental mode Rayleigh wave on VSGs. As an averaged velocity, we set 1100 m/s based on the dispersion spectrum generated along Pollock Rd (Fig. 3) and the velocity model in Czarny and Zhu (2022). We operate on the VSGs stacked over one month July 2019, when the SNR is the highest. We do not apply f-k filtering to analyze all effects around the fiber. We set the 600×1000 m grid and the limit frequency band to 10–45 Hz. We constrain our analysis to 200 m around VS. We evaluate VSG every 10 meters (VS point locations as in the case of temporal studies).

Figure 7 shows 12 selected VS points for noise source spatial distribution analysis. The results for all 80 VS points are presented in supplementary materials. Generally, each VS point gives unique spatial noise distribution. However, for most examples, the noise source is connected with car traffic through Pollock Rd. Starting from VSG in point (1), the dominant noise source comes from the east side of Pollock Rd. The noise source may originate in the utility hole (A). At point (2), the major energy shifts to the west toward higher channels. The energy still accumulates inline and is probably connected with the right edge of the wide 20 meters long bump (B). This noise source also dominates the VSG at point (3). However, the SNR rapidly decreases when the car passes between two edges of this bump (Fig 7b). One can also see these shadow zones with lower SNR in Figures 5c and 5d. For point (4), located at the top of the bump, the other noise sources on the west start appearing (C, D). At point (5), we notice the energy which can have an origin in two intersections that lead to local parking (C). However, the most energy probably travels from few utility holes (D) and two bumps (E). The high contribution of obstacle (D) in noise generation in the area is visible on VSG around 200 m (points (5) and (6)). It is worth noting that between bump (B) and the first STOP sign (around 400 m), cars drive smoothly at the highest speed along Pollock Rd. That is probably why the SNRs in this region are high. At point (8), we still observe some energy from bumps (E) and some inline noise from the west where manhole (F) is localized. This maintenance hole is in the center of the road, and almost every car hits it when driving. The SNRs for the next following VSGs decrease and reach a minimum of around 600 m.

We have several STOP signs from 400 m to the intersection with Burrowes Rd, so cars drive slower in this segment. Therefore, some off-axis sources, like traffic along Fraser Rd (G), the road to local parking (G), or more distant Burrowes Rd (H), can disturb the retrieving surface wave. We cannot exclude the impact of local lateral structural changes in dolomite bedrock or another noise source from nearby facilities. Finally, at points (11) and (12), the noise energy focuses on Burrowes Rd and N Atherton St, respectively.

5 Conclusions

We characterized high-frequency seismic ambient noise in the urban area in the city of State College using a straight roadside dark fiber DAS array and the seismic interferometry method. By analyzing the SNR estimated for VS points for every 10 m along the fiber optic cable, we identified the origin of the seismic ambient noise sources in the area and showed its spatial distribution. We also explained the factors that impact the Rayleigh surface wave estimation

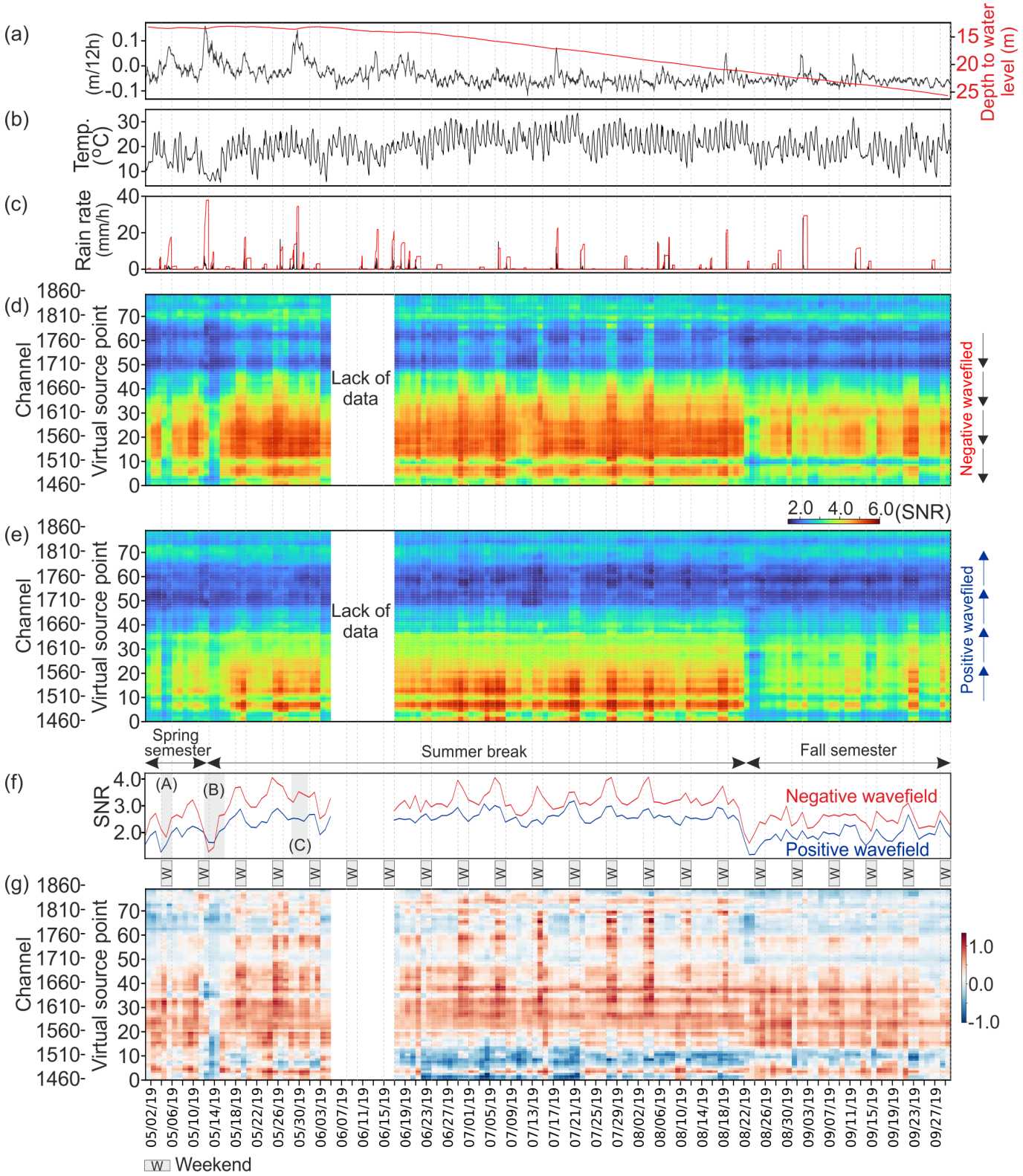

Figure 5 (a) Depth to water level from the nearest observation well; (b) Temperature and (c) rain rate from the local meteorological station (Fig. 1); SNR of the estimated Rayleigh surface wave for (d) negative and (e) positive wavefields. (f) SNR averaged for all VS points. (g) The difference between (d) and (e).

from ambient noise interferometry. We observed a significant SNR drop due to rain and pedestrian traffic. The high-quality data we get for virtual source points close to bumps and maintenance holes, particularly in region where cars are driving at higher speeds. The presented processing scheme can be applied to different sites, especially for the city's linear fiber optic array geometry. Our results can be helpful in ambient noise interferometry applications for higher frequency surface wave estimation in the city using DAS.

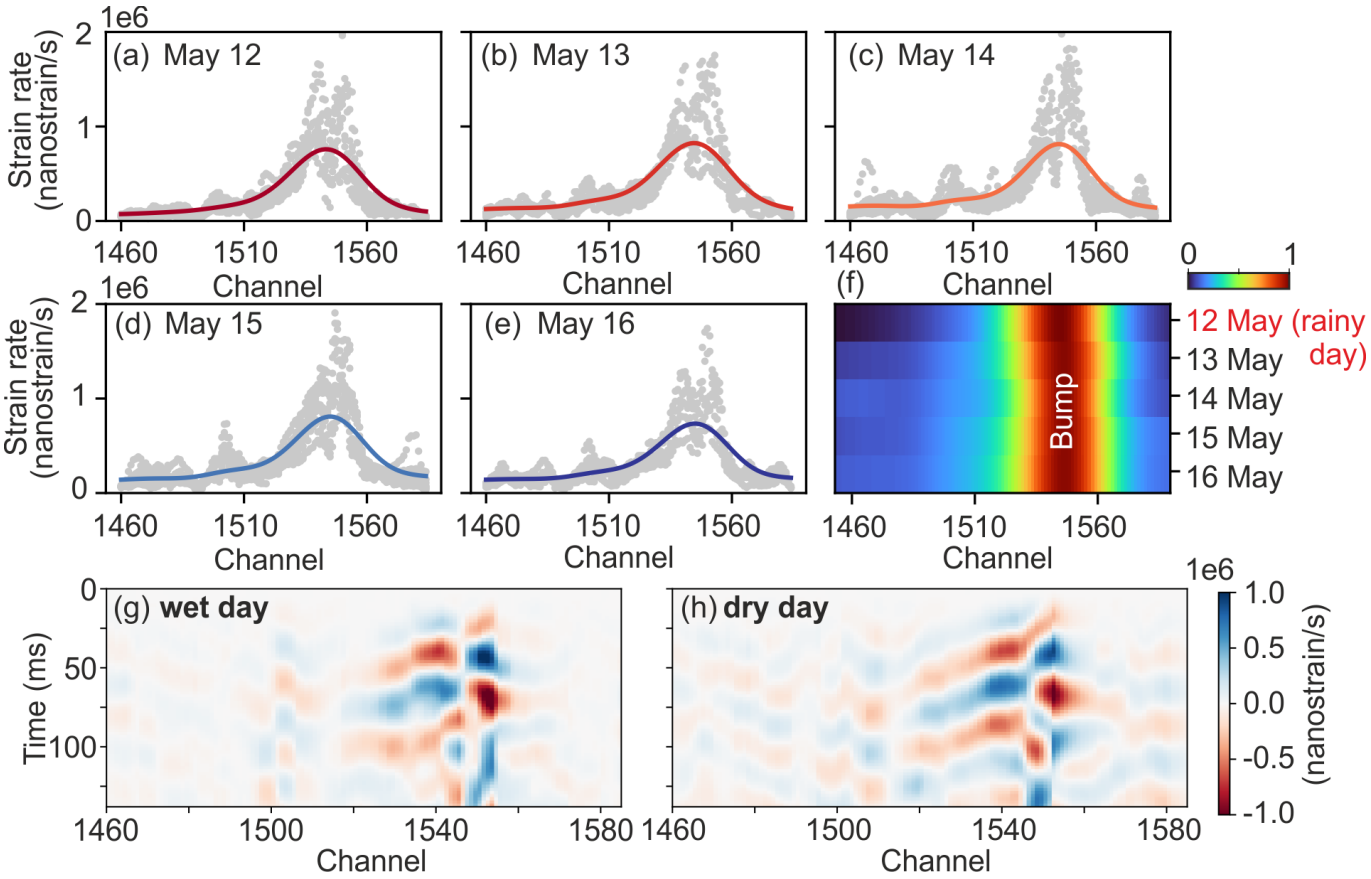

Figure 6 (a-e) Rayleigh surface wave amplitude distributions around the selected bump at channel 1560 for different days of May. (f) Comparison of the results from (a) to (f). Raw waveforms for similar source energy (comparable car hits) on wet (g) and dry (h) days. The higher attenuation is visible on a wet day.

Acknowledgements

The Penn State FORESEE array was supported by Penn State Institute of Environment and Energy seed grant and Institute of Natural Gas Research. We acknowledge the financial support from the Department of Energy (DOE) grant DE-FE0032058 and the National Science Foundation under Grants CMMI-2034363 and RISE-2228314.

Data and code availability

FORESEE data is available via PubDAS Globus https://app.globus.org/filemanager?origin_id=706e304c-5def-11ec-9b5cf9dfb1abb183&originpath=%2F Spica et al. (2022). The processing codes one can find at https://github.com/ravczarny/foresee_data_proc.git.

Competing interests

The authors have no competing interests.

References

Ajo-Franklin, J. B., Dou, S., Lindsey, N. J., Monga, I., Tracy, C., Robertson, M., Rodriguez Tribaldos, V., Ulrich, C., Freifeld, B., Daley, T., and Li, X. Distributed Acoustic Sensing Using Dark Fiber for Near-Surface Characterization and Broadband Seismic Event Detection. *Scientific Reports*, 9(1):1328, Feb. 2019. doi: 10.1038/s41598-018-36675-8.

Bensen, G., Ritzwoller, M., Barmin, M., Levshin, A., Lin, F., Moschetti, M., Shapiro, N., and Yang, Y. Processing seismic ambient noise data to obtain reliable broad-band surface wave dispersion measurements. *Geophysical Journal International*, 169: 1239–1260, 2007. doi: 10.1111/j.1365-246X.2007.03374.x.

Czarny, R. and Zhu, T. Estimating Rayleigh surface wave from ambient noise recorded by Distributed Acoustic Sensing (DAS) dark fiber array in the city. *SEG Technical Program Expanded Abstracts*, page 2133–2137, 2022. doi: 10.1190/image2022-3750564.1.

Dou, S., Lindsey, N., Wagner, A., Daley, T., Freifeld, B., Robertson, M., Peterson, J., Ulrich, C., Martin, E., and Ajo-Franklin, J. Distributed Acoustic Sensing for Seismic Monitoring of the Near Surface: A Traffic-Noise Interferometry Case Study. *Scientific Reports*, 7(1):1–12, 2017. doi: 10.1038/s41598-017-11986-4.

Drake, J. and Harmon, R. Hydrochemical environments of carbonate terrains. *Water resources research*, 9(4):949–957, 1973.

Díaz, J., Ruiz, M., Sánchez-Pastor, P., and Romero, P. Urban Seismology: On the origin of earth vibrations within a city. *Scientific Reports*, 7(1):1–11, 2017. doi: 10.1038/s41598-017-15499-y.

Fang, G., Li, Y., Zhao, Y., and Martin, E. Urban Near-Surface Seismic Monitoring Using Distributed Acoustic Sensing. *Geophysical Research Letters*, 47(6):1–9, 2020. doi: 10.1029/2019GL086115.

Li, L., Tan, J., Schwarz, B., Staněk, F., Poiata, N., Shi, P., and Gajewski, D. Recent advances and challenges of waveform-based seismic location methods at multiple scales. *Reviews of Geophysics*, 58(1), 2020. doi: 10.1029/2019rg00066.

Li, Y., Karrenbach, M., and Ajo-Franklin, J. *Distributed acoustic sensing in geophysics: Methods and applications (268*. John Wiley and Sons, 2022.

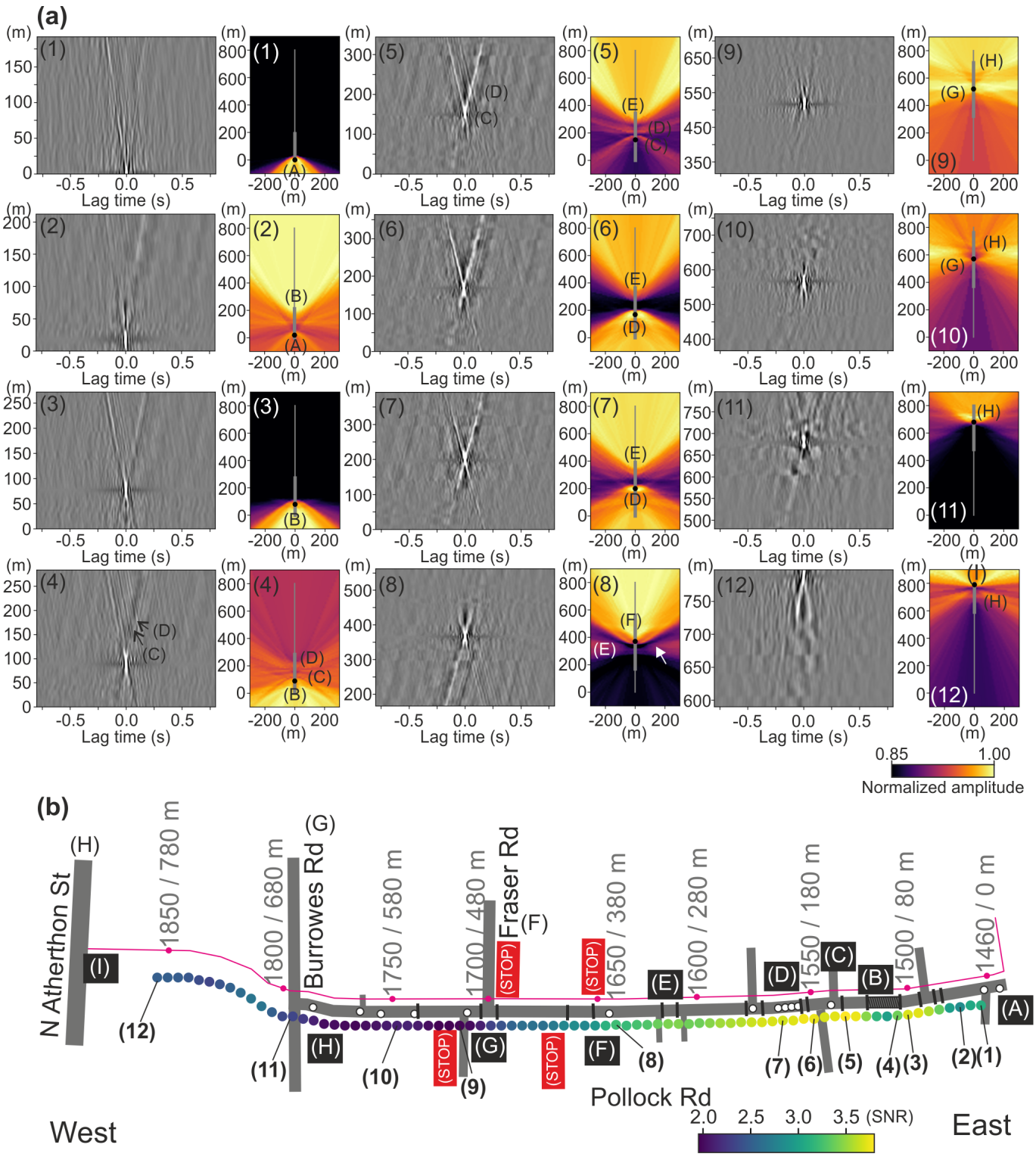

Figure 7 (a) Spatial distribution on noise source around the fiber optic cable for 12 selected VSGs. Thin and thick gray lines indicate an 800 m DAS array (channels 1460–1860) and the profile for which the spatial distribution of noise is determined, respectively. (b) Pollock Rd with road infrastructure (A-I). SNR is averaged from five months for positive and negative wavefields (Fig. 5d and 5e).

Lindsey, N. and Martin, E. Fiber-Optic Seismology. *Annual Review of Earth and Planetary Sciences*, 49(1):1–35, 2021. doi: 10.1146/annurev-earth-072420-065213.

Martin, E., Lindsey, N., and Biondi, B. Introduction to Interferometry of Fiber Optic Strain Measurements. *EarthArXiv*, 2:1–33, 2018. doi: 10.31223/osf.io/s2tjd.

Nakata, N., Chang, J., Lawrence, J., and Boué, P. Body wave extraction and tomography at Long Beach, California, with ambient-noise interferometry. *Journal of Geophysical Research: Solid Earth*, 120(2):1159–1173, 2015. doi: 10.1002/2015JB011870.

Nakata, N., Gualtieri, L., and Fichtner, A. *Seismic ambient noise*. Cambridge University Press, 2019.

Nayak, A. and Ajo-Franklin, J. Distributed Acoustic Sensing Using Dark Fiber for Array Detection of Regional Earthquakes. *Seismological Research Letters*, 92(4):2441–2452, 2021. doi: 10.1785/0220200416.

Paitz, P., Edme, P., Gräff, D., Walter, F., Doetsch, J., Chalari, A., and Fichtner, A. Empirical investigations of the instrument response for distributed acoustic sensing (DAS) across 17 octaves. *Bulletin of the Seismological Society of America*, 111(1):1–10, 2021. doi: 10.1785/0120200185.

Rabade, S., Wu, S., Lin, F., and Chambers, D. Isolating and Tracking Noise Sources across an Active Longwall Mine Using Seismic Interferometry. *Bulletin of the Seismological Society of America*, 112(5):2396–2407, 2022. doi: 10.1785/0120220031.

Shen, J. and Zhu, T. Seismic noises by telecommunication fiber optics reveal the impact of COVID-19 measures on human activities. *The Seismic Record*, 1(1):46–55, 2021. doi: 10.1785/0320210008.

Shen, J. and Zhu, T. DAS with telecommunication fiber-optic cable in urban areas can record storm-induced seismic noise, 2023. GJI, submitted.

Song, Z., Zeng, X., Xie, J., Bao, F., and Zhang, G. Sensing Shallow Structure and Traffic Noise with Fiber-optic Internet Cables in an Urban Area. *Surveys in Geophysics*, 42(6):1401–1423, 2021. doi: 10.1007/s10712-021-09678-w.

Song, Z., Zeng, X., Chi, B., Bao, F., and Osotuyi, A. Using the three-station interferometry method to improve urban DAS ambient noise tomography. *Frontiers in Earth Science*, 10, 2022. doi: 10.3389/feart.2022.952410.

Spica, Z., Perton, M., Martin, E., Beroza, G., and Biondi, B. Urban Seismic Site Characterization by Fiber-Optic Seismology. *Journal of Geophysical Research: Solid Earth*, 125(3):1–14, 2020. doi: 10.1029/2019JB018656.

Spica, Z., J., A.-F., C., B. G., B., B., F., C., B., G., B., L., E., M., J., S., C., T., L., V., H., W., A., W., H., X., and T, Z. PubDAS: a PUBlic Distributed Acoustic Sensing1datasets repository for geosciences. *EarthArXiv*, 2022. doi: 10.31223/X5D07S.

Titov, A., Fan, Y., Kutun, K., and Jin, G. Distributed Acoustic Sensing (DAS) Response of Rising Taylor Bubbles in Slug Flow. *Sensors*, 22(3), 2022. doi: 10.3390/s22031266.

Tribaldos, V. and Ajo-Franklin, J. Aquifer Monitoring Using Ambient Seismic Noise Recorded with Distributed Acoustic Sensing (DAS) Deployed on Dark Fiber. *Journal of Geophysical Research: Solid Earth*, page 1–20, 2021. doi: 10.1029/2020jb021004.

van den Ende, M. and Ampuero, J. Evaluating seismic beamforming capabilities of distributed acoustic sensing arrays. *Solid Earth*, 12(4):915–934, 2021. doi: 10.5194/se-12-915-2021.

Vidal, C., Draganov, D., Neut, J., Drijkoningen, G., and Wapenaar, K. Retrieval of reflections from ambient noise using illumination diagnosis. *Geophysical Journal International*, 198(3):1572–1584, 2014. doi: 10.1093/gji/ggu164.

Wapenaar, K., Draganov, D., and Snieder, R. Tutorial on seismic interferometry: Part 1 - Basic principles and applications. *Geophysics*, 75:75 195–75 209, 2010. doi: 10.1190/1.3457445.

Yang, Y., Atterholt, J., Shen, Z., Muir, J., Williams, E., and Zhan, Z. Sub-Kilometer Correlation Between Near-Surface Structure and Ground Motion Measured With Distributed Acoustic Sensing. *Geophysical Research Letters*, 49(1), 2022. doi: 10.1029/2021GL096503.

Zeng, X., Lancelle, C., Thurber, C., Fratta, D., Wang, H., Lord, N., Chalari, A., and Clarke, A. Properties of noise cross-correlation functions obtained from a distributed acoustic sensing array at Garner Valley, California. *Bulletin of the Seismological Society of America*, 107(2):603–610, 2017. doi: 10.1785/0120160168.

Zhu, T., Shen, J., and Martin, E. Sensing Earth and environment dynamics by telecommunication fiber-optic sensors: An urban experiment in Pennsylvania, USA. *Solid Earth*, 12(1):219–235, 2021. doi: 10.5194/se-12-219-2021.